

1 **Physics-Informed Neural Networks for fault slip monitoring: simulation, frictional**
2 **parameter estimation, and prediction on slow slip events in a spring-slider system**

3 **Rikuto Fukushima¹, Masayuki Kano², and Kazuro Hirahara^{3,4}**

4 ¹ Faculty of Science, Kyoto University, Kyoto, Japan.

5 ² Graduate School of Science, Tohoku University, Sendai, Japan.

6 ³ RIKEN Center for Advanced Intelligence Project, Seika, Japan.

7 ⁴ Kagawa University, Takamatsu, Japan.

8 Corresponding author: Rikuto Fukushima (fukushima.rikuto.27n@st.kyoto-u.ac.jp) and Masayuki
9 Kano (masayuki.kano.a3@tohoku.ac.jp)

10

11 **Key Points:**

- 12 • We propose Physics-Informed Neural Networks (PINNs) for fault slip simulation,
13 frictional parameter estimation, and slip prediction.
- 14 • PINNs can reproduce slow slip events in a spring-slider system and estimate the frictional
15 parameters from synthetic observation data.
- 16 • We investigated the potential of the predictability of subsequent fault slips from limited
17 observation data including uncertainties.

18

19 **Abstract**

20 The episodic transient fault slips called slow slip events (SSEs) have been observed in many
21 subduction zones. These slips often occur in regions adjacent to the seismogenic zone during the
22 interseismic period, making monitoring SSEs significant for understanding large earthquakes.
23 Various fault slip behaviors, including SSEs and earthquakes, can be explained by the spatial
24 heterogeneity of frictional properties on the fault. Therefore, estimating frictional properties from
25 geodetic observations and physics-based models is crucial for fault slip monitoring. In this study,
26 we propose a Physics-Informed Neural Network (PINN)-based new approach to simulate fault slip
27 evolutions, estimate frictional parameters from observation data, and predict subsequent fault slips.
28 PINNs, which integrate physical laws and observation data, represent the solution of physics-based
29 differential equations. As a first step, we validate the effectiveness of the PINN-based approach
30 using a simple single-degree-of-freedom spring-slider system to model SSEs. As a forward
31 problem, we successfully reproduced the temporal evolution of SSEs using PINNs and obtained
32 implications on how to choose the appropriate collocation points by analyzing the residuals of
33 physics-based differential equations. As an inverse problem, we estimated the frictional parameters
34 from synthetic observation data and demonstrated the ability to obtain accurate values regardless
35 of the choice of first-guess values. Furthermore, we discussed the potential of the predictability of
36 the subsequent fault slips using limited observation data, taking into account uncertainties. Our
37 results indicate the significant potential of PINNs for fault slip monitoring.

38

39 **Plain Language Summary**

40 Slow slip events (SSEs), which are fault slips characterized by slower velocity and longer duration
41 compared to earthquakes, have been observed in many subduction zones. Monitoring SSEs is
42 important for understanding large earthquakes because they occur adjacent to areas where
43 significant earthquakes could potentially occur. Different types of fault slips, including SSEs and
44 earthquakes, can be explained by distinct frictional properties on the fault. These frictional
45 properties can be estimated from physical laws of fault slip and observed crustal deformation. In
46 this study, we propose a new machine-learning based approach for fault slip monitoring. We
47 employed Physics-Informed Neural Networks (PINNs), which simultaneously learn the physical
48 laws and data, to simulate fault slip, estimate the frictional parameters, and predict subsequent
49 fault slip. As a first step, we utilized a single-degree-of-freedom spring-slider system, which is the
50 simplest physical model to simulate SSEs. We successfully simulated SSEs, estimated frictional
51 properties from synthetic observation data, and discussed the potential for fault slip prediction.
52 Our results suggest the significant potential of PINNs for fault slip monitoring.

53

54 **1 Introduction**

55 Recent geophysical observations have revealed that faults episodically slip slowly during
56 the interseismic period (e.g., Hirose et al., 1999). These episodic slow fault slips, known as slow
57 slip events (SSEs), have been observed in many subduction zones. SSEs repeatedly occur in
58 regions adjacent to possible source areas of large earthquakes (Obara & Kato, 2016). Moreover,
59 SSEs have been considered to share common physical mechanisms with large earthquakes.
60 Therefore, it is crucial to monitor these slow fault slip phenomena and understand the generation
61 mechanisms of SSEs.

62 Various fault slip behaviors, including SSEs and earthquakes, can be explained by distinct
63 frictional properties on the fault (e.g., Yoshida & Kato, 2003). For fault slip monitoring, it is crucial
64 to estimate the frictional properties from current geodetic observations and predict fault slip
65 evolutions based on physics-based models. Incorporating fault friction in the model enables us to
66 simulate the spatio-temporal evolution of fault slip on the megathrust. In these simulations, the
67 quasi-dynamic equation of motion (Rice, 1993), and a rate and state dependent friction (RSF) law
68 (Dieterich, 1979), derived empirically from laboratory experiments, are frequently employed.
69 Various fault slips can be reproduced by appropriately setting three frictional parameters (a , $a-b$,
70 and d_c) that control the frictional properties on the fault in RSF. In such simulations, the frictional
71 parameters are determined by trial and error to qualitatively reproduce the observed fault slips due
72 to the difficulty of directly measuring these frictional parameters.

73 Therefore, for fault slip monitoring, it is vital to determine the appropriate frictional
74 parameters by combining observations and physics-based models. To achieve this, data
75 assimilations have been employed to investigate frictional parameters from observed slip velocities
76 of afterslip (Kano et al., 2015; 2020) and long-term SSEs (Hirahara & Nishikiori, 2019). Kano et
77 al. (2020) estimated frictional parameters from observed crustal deformation following the 2003
78 Tokachi-oki earthquake and predicted subsequent fault slips and crustal deformation. These
79 studies confirmed that data assimilations enable the optimization of unknown frictional parameters
80 on faults based on observed crustal deformation and physics-based models. It should be noted that
81 these studies mainly focused on investigating the potential of data assimilations by assuming that
82 RSF is the true physics of SSEs. However, the physical mechanism of SSEs still remains
83 controversial with other possible mechanisms such as dilatant strengthening (e.g., Segall et al.,

84 2010) and the transition from rate-strengthening friction to rate-weakening friction at higher slip
85 rates (e.g., Im et al., 2020).

86 In this paper, we propose a new machine learning-based approach to simulate fault slip
87 evolutions, estimate frictional parameters from observation data, and predict subsequent fault slips
88 using the estimated frictional parameters. With recent advancements in machine learning, Physics-
89 Informed Neural Networks (PINNs) have been proposed as a new deep learning method for data-
90 driven solutions of partial differential equations as forward problems, as well as for the data-driven
91 discovery of partial differential equations as inverse problems to investigate parameters that best
92 describe the observed data (Raissi et al., 2019). This method involves constructing neural networks
93 capable of solving physics-based equations by minimizing a loss function that incorporates
94 differential equations and initial/ boundary conditions. This approach has been recently employed
95 in numerous research fields as it provides a mesh-free framework for forward problems and
96 provides effective solutions for inverse problems. In seismology, PINNs have been employed in
97 various problems, including travel time calculation (Smith et al., 2021a and Waheed et al., 2021a),
98 hypocenter inversion (Smith et al., 2021b), full-waveform inversion (Rasht-Behesht et al., 2022),
99 seismic tomography (Waheed et al., 2021b and Agata et al., 2023), and modeling crustal
100 deformation (Okazaki et al., 2022).

101 The PINN-based method for fault slip monitoring has the advantages of its extendibility
102 and flexibility compared to conventional data assimilation methods such as adjoint method (Kano
103 et al., 2015; 2020) and Ensemble Kalman filter (Hirahara and Nishikiori, 2019) and will be
104 expected especially when we apply to the more realistic subduction zones including crustal
105 heterogeneity and nonlinear viscoelasticity. The PINN-based calculation under the different
106 physics models can be completed simply by changing the definition of loss functions, making it

107 easy to consider the complex models, especially in the inversion. For example, in the previous
108 frictional parameter estimation using data assimilation methods (e.g., Kano et al., 2015; 2020 and
109 Hirahara and Nishikiori, 2019), they used analytical slip response functions available only for
110 simple media such as the homogeneous elastic half space and ignored the effect of crustal
111 heterogeneity and nonlinear viscoelasticity in the mantle, whose slip response functions can be
112 obtained only by fully numerical methods such as finite element methods. In contrast, the PINN-
113 based method can calculate the solution without any slip response functions by learning the physics
114 considering heterogeneous nonlinear viscoelastic media, providing us with a more simple
115 inversion method considering the realistic situation than conventional data assimilation techniques.

116 Taking into consideration such extendibility of the PINN-based inversion, this study first
117 applies PINNs to the simulation of slip evolution on faults and develops the fundamental
118 methodology under a simple model. As stated before, there exist a variety of slip evolutions
119 producing SSEs and earthquakes with fast slip rates. In this paper, we focus on SSEs, because their
120 slip behaviors are rather stable and can be easily simulated compared to earthquakes. Many
121 numerical studies on SSEs have so far been executed assuming realistic structures such as
122 subduction zones. In this study, as a first step, we utilize a single-degree-of-freedom spring-slider
123 system (Yoshida & Kato, 2003), which is the simplest physical model to calculate temporal
124 evolutions of SSEs. The objectives of this study are as follows: (i) simulating the temporal
125 evolutions of SSE as a forward problem, (ii) estimating the frictional parameters from observed
126 slip velocity data as an inverse problem, and (iii) predicting the future evolution of SSE, including
127 quantifying the uncertainty associated with each result. Through these calculations, we aim to
128 verify that our new PINN-based approach is a powerful tool for simulating slip evolutions,
129 estimating frictional parameters, and predicting fault slip evolutions.

130 The paper is organized as follows. Section 2 explains the fault slip model based on the RSF
131 law and presents the results of conventional numerical calculations. Section 3 demonstrates the
132 forward calculations of the temporal evolution of SSE using the PINN-based approach. In Section
133 4, we estimate the frictional parameters from synthetic observation data, considering their
134 uncertainties. Finally, in Section 5, we attempt to predict subsequent evolution of SSE from limited
135 observation data and discuss the relationship between the uncertainties of the estimated parameters
136 and the length of the observation data.

137

138 **2 Conventional Numerical Simulation**

139 We initiate the study by conducting a numerical simulation to obtain the temporal evolution
140 of fault slips. This simulation serves as a reference for comparing results obtained using the PINN-
141 based approach. We adopt a single degree-of-freedom spring-slider model (Yoshida & Kato, 2003),
142 which comprises a block and a spring (Figure 1a). In this system, the block is loaded with a
143 constant velocity. By assuming the frictional properties between the block and the surface, we can
144 represent various fault slips ranging from slow to fast slips on the block. The quasi-dynamic
145 equation of motion in this model is expressed as:

$$146 \quad \tau = k (v_{pl} t - x) - \eta v, \quad (1)$$

147 where τ is the shear stress, k is the stiffness of the spring, v_{pl} is the loading velocity, t is the time,
148 and x is the accumulated slip of the block. The second term on the right-hand side represents a
149 radiation damping approximation (Rice, 1993), which was introduced to express the stress-release
150 by the radiation of seismic waves instead of the inertia term. The coefficient η is expressed as $\eta =$

151 $\mu / 2v_s = 5 \times 10^6$ [Pa s/m], where the shear modulus μ is 3.0×10^{10} [Pa] and shear wave velocity v_s
 152 is 3×10^3 [m/s].

153 The RSF law (Dieterich, 1979) is often employed to express fault friction. The frictional
 154 stress τ is expressed as

$$155 \quad \tau = \sigma \left(f_0 + a \log \left(\frac{v}{v_{pl}} \right) + b \log \left(\frac{\theta v_{pl}}{d_c} \right) \right), \quad (2)$$

156 where θ is the state variable, σ is the normal stress, f_0 is a frictional coefficient, and a , b , and d_c are
 157 the frictional parameters. These frictional parameters express the frictional properties of faults. If
 158 $a - b > 0$, the friction becomes rate-strengthening and if $a - b < 0$, the friction becomes rate-
 159 weakening, which makes the system unstable. The instability of the model is determined by the
 160 frictional parameters, spring stiffness k , and critical stiffness k_{crit} (Ruina, 1983) defined as:

$$161 \quad k_{crit} = \frac{\sigma (b - a)}{d_c}. \quad (3)$$

162 When k is larger than k_{crit} , the system exhibits strong instability and behaves like fast earthquakes.
 163 When $k < k_{crit}$ and $k \approx k_{crit}$, the system shows a slow transient motion like SSEs. The state variable
 164 characterizes the state of the fault surface and several laws were proposed to describe the temporal
 165 evolution of the state variable. Here, we used the aging law (Ruina, 1983) described as:

$$166 \quad \frac{d\theta}{dt} = 1 - \frac{\theta v}{d_c}. \quad (4)$$

167 By combining these equations Eqs. (1), (2), and (4), we can calculate the temporal
 168 evolution of slip velocity v and state variable θ . We non-dimensionalized these equations by
 169 defining:

170
$$p = \log\left(\frac{v}{v_{pl}}\right), \quad (5)$$

171
$$q = \log\left(\frac{\theta v_{pl}}{d_c}\right). \quad (6)$$

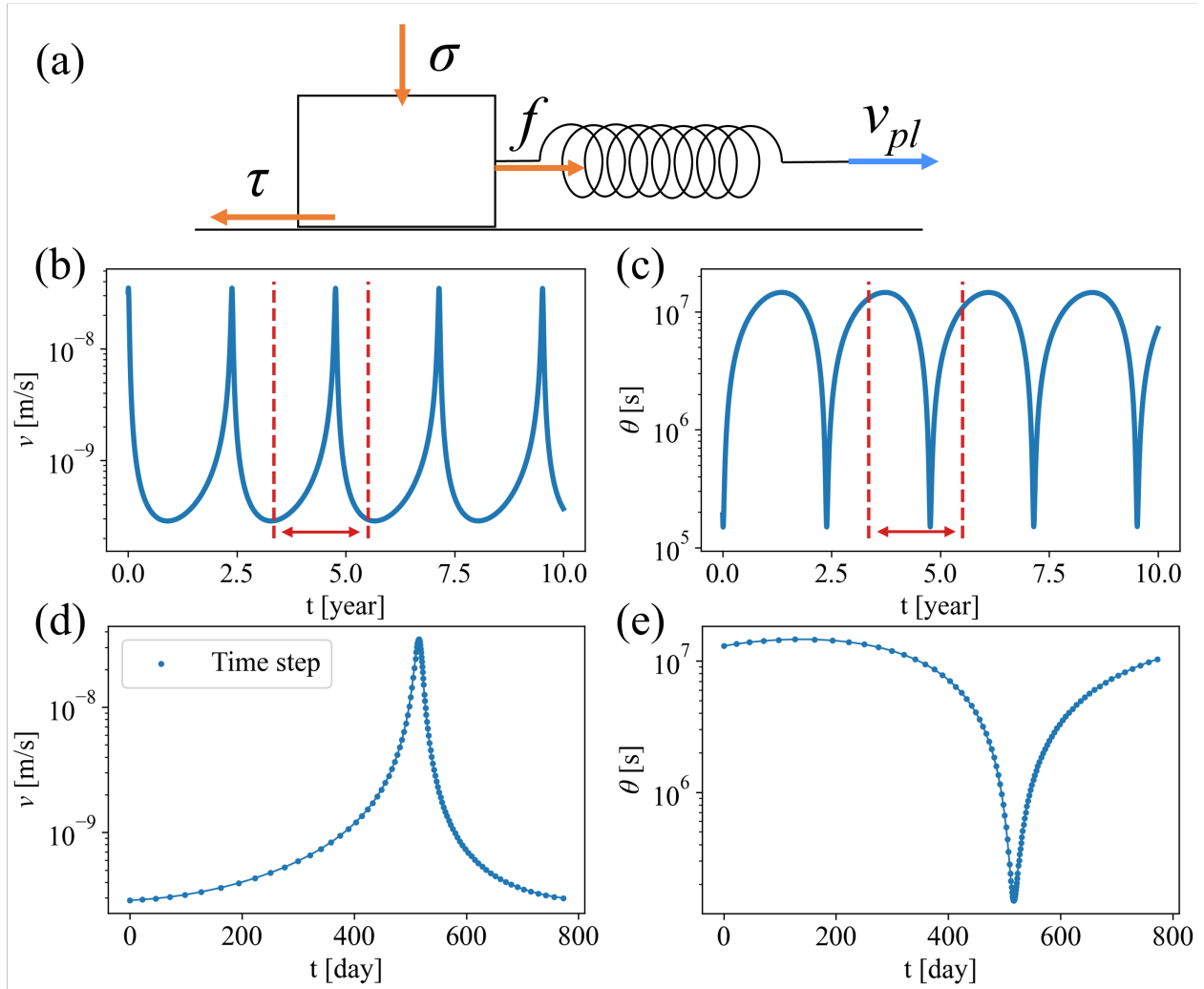
172 Then the target equations are written as:

173
$$\frac{dp}{dt} = (a\sigma + \eta v_{pl} e^p)^{-1} \left(kv_{pl}(1 - e^p) - \frac{b\sigma v_{pl}}{d_c} (e^{-q} - e^p) \right), \quad (7)$$

174
$$\frac{dq}{dt} = \frac{v_{pl}}{d_c} (e^{-q} - e^p). \quad (8)$$

175 We set the frictional parameters a , b , and d_c , and normal stress σ to reproduce the SSE as
 176 $a = 1 \times 10^{-4}$, $a-b = -1 \times 10^{-5}$, $d_c = 5 \times 10^{-3}$ [m], and $\sigma = 10^7$ [Pa]. The spring stiffness k is set to
 177 satisfy $k / k_{crit} = 0.9999$, which is required to cause the transient motion. We set the loading rate v_{pl}
 178 $= 5$ [cm/yr] $= 1.58 \times 10^{-9}$ [m/s]. The temporal evolution of slip velocity under these parameters
 179 was calculated by the 5th-order time-adaptive Runge–Kutta (RK) method with a tolerance of 10^{-8} .
 180 Figures 1b and 1c display the temporal evolutions of slip velocity v and state variable θ . The
 181 simulation results showed a maximum slip velocity of $\sim 10^{-8}$ [m/s], a cumulative slip of ~ 10 cm,
 182 and recurrence intervals of SSEs of 2.5 years. These characteristics are similar to the Tokai slow
 183 slip events in the first-order approximation (Miyazaki et al., 2006). Hereafter we will use this result
 184 as a reference, aiming to calculate the temporal evolution of SSE in one cycle.

185



186

187 **Figure 1.** (a) Schematic illustration of a spring-slider model. (b-e) Results of conventional
 188 numerical calculation. (b)(c) Temporal evolutions of (b) slip velocity v and (c) state variable θ for
 189 several cycles. (d)(e) Enlarged view of (b) and (c) focusing on one cycle indicated by red lines in
 190 (b) and (c). Blue points show the time steps used in the time-adaptive RK method.

191

192 3 Forward Problem

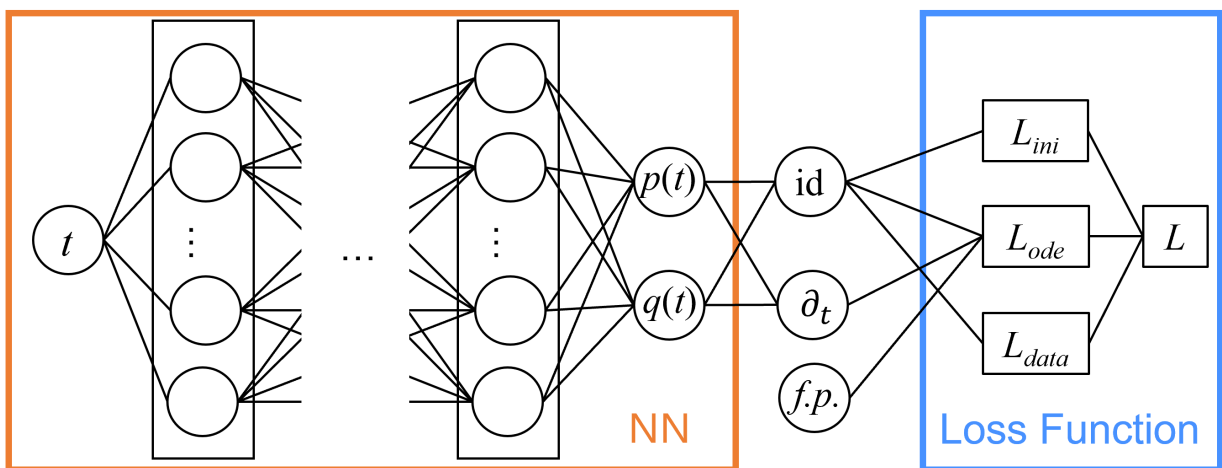
193 In this section, we describe how to model the fault slips in a spring-slider model using the
 194 PINN-based approach and discuss the results.

195

196 **3.1 Method**

197 A neural network was constructed to model the temporal evolutions of $p(t)$ and $q(t)$ (Figure
 198 2). The network uses an input layer with one node corresponding to time t , and an output layer
 199 with two nodes corresponding to $p(t)$ and $q(t)$. It has a nine-layer fully connected neural network
 200 and uses the hyperbolic tangent as the activation function. The number of intermediate layers is
 201 eight with twenty nodes each. In total, the neural network has 162 biases and 2860 weights, and
 202 we can solve the differential equations by optimizing these neural network parameters. We follow
 203 the original framework of PINNs (Raissi et al., 2019) to construct this neural network
 204 configuration. In this study, the network biases are initialized to zero, and the network weights are
 205 initialized by normal Xavier initialization (Glorot & Bengio, 2010), which is widely used in PINNs.
 206 In this initialization method, the weights are selected from the Gaussian distribution to keep the
 207 variance of the output the same across every layer.

208



209

210 **Figure 2.** Structure of PINNs. The neural networks have an input, time t , and the corresponding
 211 outputs $p(t)$ and $q(t)$. The loss function L is calculated by using the frictional parameters ($f.p.$) and
 212 operating the identity function (id) and the time derivation (∂_t) to p and q . In Section 3, we solve
 213 the forward problem using L_{ini} (Eq. (12)) and L_{ode} (Eq. (13)). We introduce L_{data} (Eq. (15)) in the
 214 inversion in Sections 4 and 5. L_{ini} , L_{ode} , and L_{data} represent the residuals for the initial condition,
 215 governing equation, and observation data, respectively.

216

217 In the PINNs, the neural networks learn the behavior of the equation by defining the loss
 218 function considering the misfit between target equations and derivatives of the network output
 219 calculated by automatic differentiation. In this problem, we define the residuals of the differential
 220 equations as:

$$221 \quad r_p(t) = \frac{dp_{NN}}{dt} - (a\sigma + \eta v_{pl} e^{p_{NN}})^{-1} \left(kv_{pl}(1 - e^{p_{NN}}) - \frac{b\sigma v_{pl}}{d_c} (e^{-q_{NN}} - e^{p_{NN}}) \right), \quad (9)$$

$$222 \quad r_q(t) = \frac{dq_{NN}}{dt} - \frac{v_{pl}}{d_c} (e^{-q_{NN}} - e^{p_{NN}}), \quad (10)$$

223 where p_{NN} and q_{NN} are the PINNs outputs. Then the loss function L is defined as:

$$224 \quad L = L_{ini} + L_{ode}, \quad (11)$$

$$225 \quad L_{ini} = (p_{NN}(0) - p_{ini})^2 + (q_{NN}(0) - q_{ini})^2, \quad (12)$$

$$226 \quad L_{ode} = \int_0^T r(t)^2 dt = \sum_{i=1}^N r(t_i)^2 \Delta t_i. \quad (13)$$

227 where $r(t_i)^2 = r_p(t_i)^2 + r_q(t_i)^2$, p_{ini} and q_{ini} are the initial conditions of p and q . As shown in Figures
 228 1b, and 1c, our simple frictional model produces the same repeating SSE cycles after several

229 unstable cycles when the numerical effect of the initial conditions disappears. Focusing on one
230 cycle (Figures 1d and 1e), we set the initial time $t = 0$ at the time when the slip velocity is lowest
231 during one cycle. The initial conditions of p_{ini} and q_{ini} were evaluated at this time $t = 0$. L_{ini} and
232 L_{ode} represent the residuals of the initial conditions and those of the governing equations,
233 respectively. L_{ode} can be calculated at the arbitrary points t_i , which are called collocation points.
234 Δt_i indicates time intervals of collocation points and N is the number of collocation points. L_{ode} is
235 defined as the discretization of the L2 norm: $\int r(t)^2 dt$, representing the residuals of governing
236 equations. We normalized L_{ode} by multiplying t^* , which represents the characteristic time in a
237 spring-slider system defined as $t^* = d_c / v_{pl}$ (Segall, 2010). Some previous research introduced the
238 weight parameter for the loss function as a hyperparameter (e.g., Linka et al., 2022). Instead of
239 introducing weight, it is generally pointed out that normalization is important in PINNs calculation
240 (e.g., Raissi et al., 2019; Rasht-Behesht et al., 2022; Okazaki et al., 2022). In our case, by
241 considering the normalization using t^* , the calculation performs well without introducing any
242 additional weight parameter and we adopted this formulation. We used the L-BFGS method (Liu
243 & Nocedal, 1989) to optimize the network weights and biases by minimizing the loss function.
244 Training is finished when the decrease in the loss function per one optimization step becomes less
245 than the predetermined threshold value of 10^{-12} .

246 To calculate L_{ode} , the selection of collocation points is required. In this study, we employed
247 two types of collocation points: equidistant and non-equidistant. Equidistant collocation points
248 have constant time intervals, while non-equidistant collocation points have adaptive time intervals.
249 The time steps of the time-adaptive RK method, as shown in Figures 1d and 1e, were chosen as
250 non-equidistant collocation points. This is based on the idea that a higher density of collocation
251 points should be selected where the slip behavior in the system equation changes rapidly. However,

252 this method can only be applied when the slip behavior is known prior to the calculation. In
253 practical situations where there is no prior knowledge of the slip behavior, equidistant collocation
254 points are used. In the RK calculation, the total number of collocation points is 103, with maximum
255 and minimum intervals of ~ 870 and ~ 10 h, respectively. For equidistant collocation points,
256 intervals are set to be ~ 100 , 200 , and 400 h with the corresponding number of points being 187,
257 94, and 47, respectively. By comparing these results, we investigate the impact of collocation point
258 sampling on the learning of neural network parameters.

259 We validate the ability of PINNs to reproduce the SSE by comparing the PINNs outputs
260 with the results derived from a conventional numerical calculation using the RK method (Figures
261 1d and 1e). To qualitatively evaluate the misfit between the PINNs outputs and the reference values,
262 we defined the relative errors (RE) as $RE = |v_{NN} - v_{RK}| / v_{RK}$ or $RE = |\theta_{NN} - \theta_{RK}| / \theta_{RK}$. Here v_{RK} and
263 θ_{RK} represent the reference values at adaptive time steps used in the RK method, whereas v_{NN} and
264 θ_{NN} represent the PINNs outputs corresponding to those times. Please note that the RE are
265 calculated at RK time steps.

266

267 **3.2 Results and discussion**

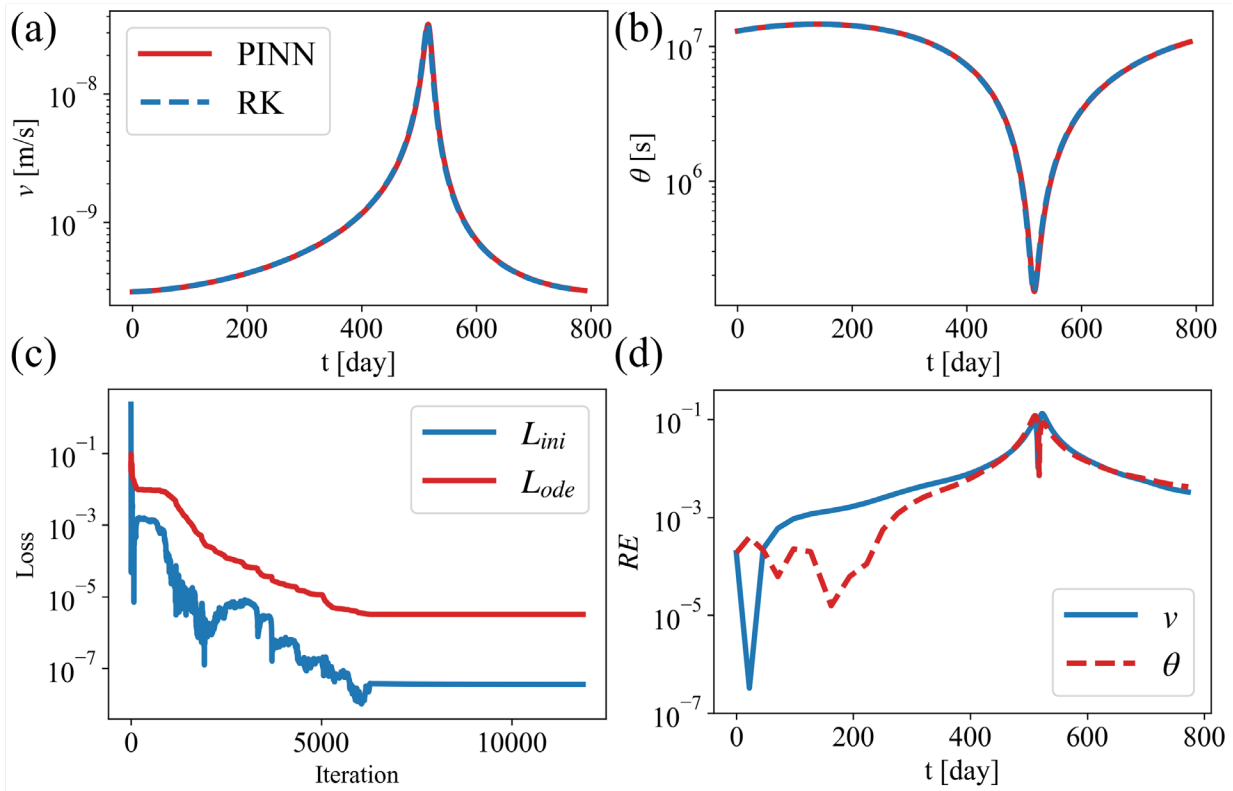
268 We solved the spring-slider problem using PINNs, applying both equidistant and non-
269 equidistant collocation points (Figures 3 and 4). Here, time intervals for equidistant collocation
270 points were set as 100 h. Note that $v_{NN}(t)$ and $\theta_{NN}(t)$ in these figures are calculated at time steps
271 with constant time intervals of 10 h, which are denser than equidistant collocation points of 100 h.
272 This is used to check the interpolation ability of PINNs. The PINNs successfully reproduced the
273 temporal evolution of SSE in both cases (Figures 3a, 3b, 4a, and 4b). The neural network

274 parameters were optimized until the number of iterations reached 11,875 and the loss function
275 yielded $L_{ini} = 3.56 \times 10^{-8}$ and $L_{ode} = 3.19 \times 10^{-6}$ for the case of equidistant collocation points (Figure
276 3c). When using non-equidistant collocation points, the number of iterations increased to 17,674,
277 with loss functions $L_{ini} = 5.21 \times 10^{-10}$ and $L_{ode} = 1.94 \times 10^{-6}$ (Figure 4c).

278 The maximum values of RE were $\sim 10^{-1}$ and $\sim 10^{-2}$ for the equidistant and non-equidistant
279 collocation points case, respectively (Figures 3d and 4d). This suggests that training with non-
280 equidistant collocation points yields more precise results than using equidistant collocation points.
281 The residuals of the governing equations, represented by $r(t)^2$ (Figures 5a and 5b), help in
282 elucidating such results. It is important to note that $r(t)^2$ differs from RE : $r(t)^2$ represents the
283 discrepancy between the time derivatives of p_{NN} and q_{NN} and the governing equations, while RE
284 represents the misfit between the PINNs outputs (v_{NN} and θ_{NN}) and the reference values (v_{RK} and
285 θ_{RK}). The scarcity of collocation points around peak velocity in the case of equidistant collocation
286 points results in larger $r(t)^2$ values compared to non-equidistant collocation points, thereby
287 increasing the difference between the output of PINNs and the reference values. These results
288 suggest that for accurate calculations, a larger number of collocation points are required at timings
289 when the slip velocity changes dramatically, which aligns with the concept of the time-adaptive
290 RK method.

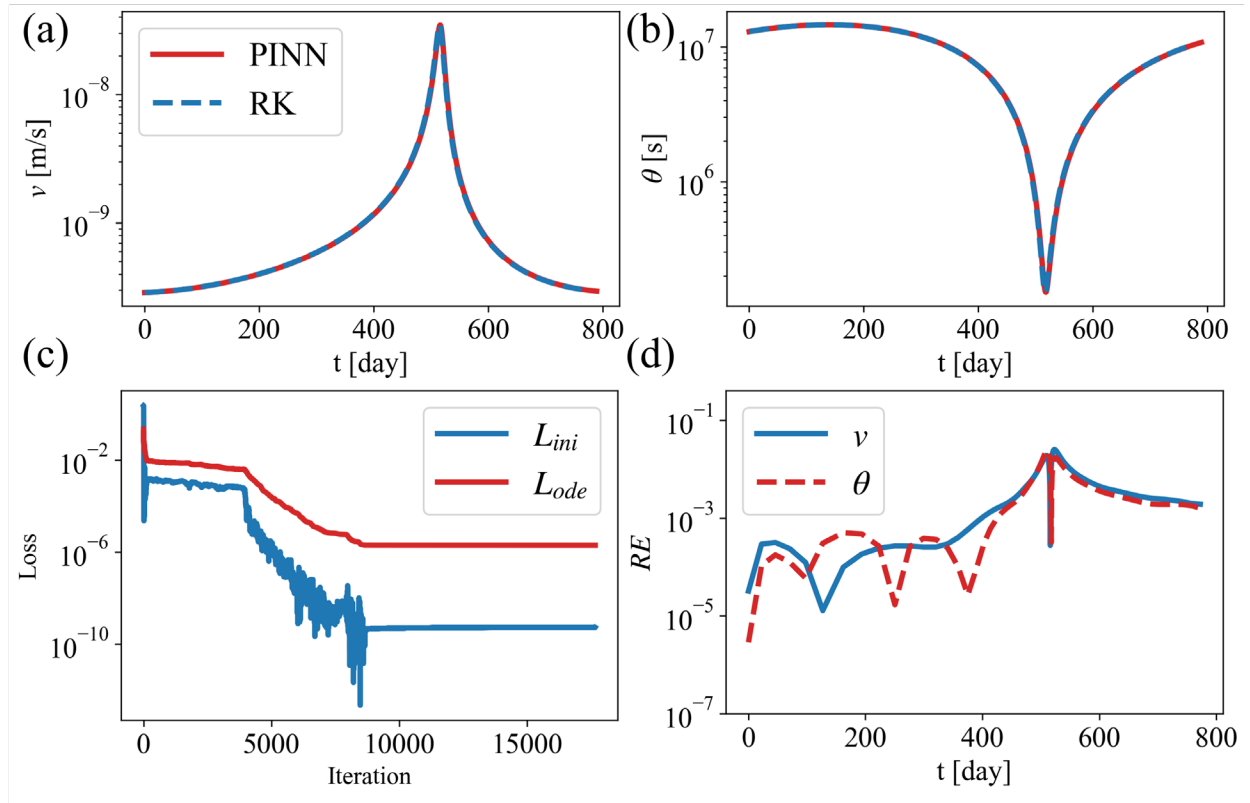
291 While the use of non-equidistant collocation points yields a more accurate RE , the
292 successful calculation of PINNs with equidistant collocation points is important to apply PINNs
293 for practical use. This is because the collocation points at peak times of slip velocity are not
294 collectable in practical use, in which prior knowledge of the solution of the equations is not
295 available. This approach ensures a feasible methodology when the temporal pattern of changes in
296 the system is unknown.

297



298

299 **Figure 3.** Calculation results using equidistant collocation points (with time intervals of 100 h). (a)
 300 and b) The temporal evolution of (a) v and (b) θ calculated by PINNs (red line) and the RK method
 301 (blue line). (c) Learning curve for L_{ini} and L_{ode} . The neural network parameters were converged
 302 after 11,875 iterations with $L_{ini} = 3.56 \times 10^{-8}$ and $L_{ode} = 3.19 \times 10^{-6}$. (d) RE of v and θ .



303

304 **Figure 4.** Calculation results using non-equidistant collocation points. (a and b) The temporal
 305 evolution of (a) v and (b) θ calculated by PINNs (red line) and the RK method (blue line). (c)
 306 Learning curve for L_{ini} and L_{ode} . The neural network parameters were converged after 17,674
 307 iterations with $L_{ini} = 5.21 \times 10^{-10}$ and $L_{ode} = 1.94 \times 10^{-6}$. (d) RE of v and θ .

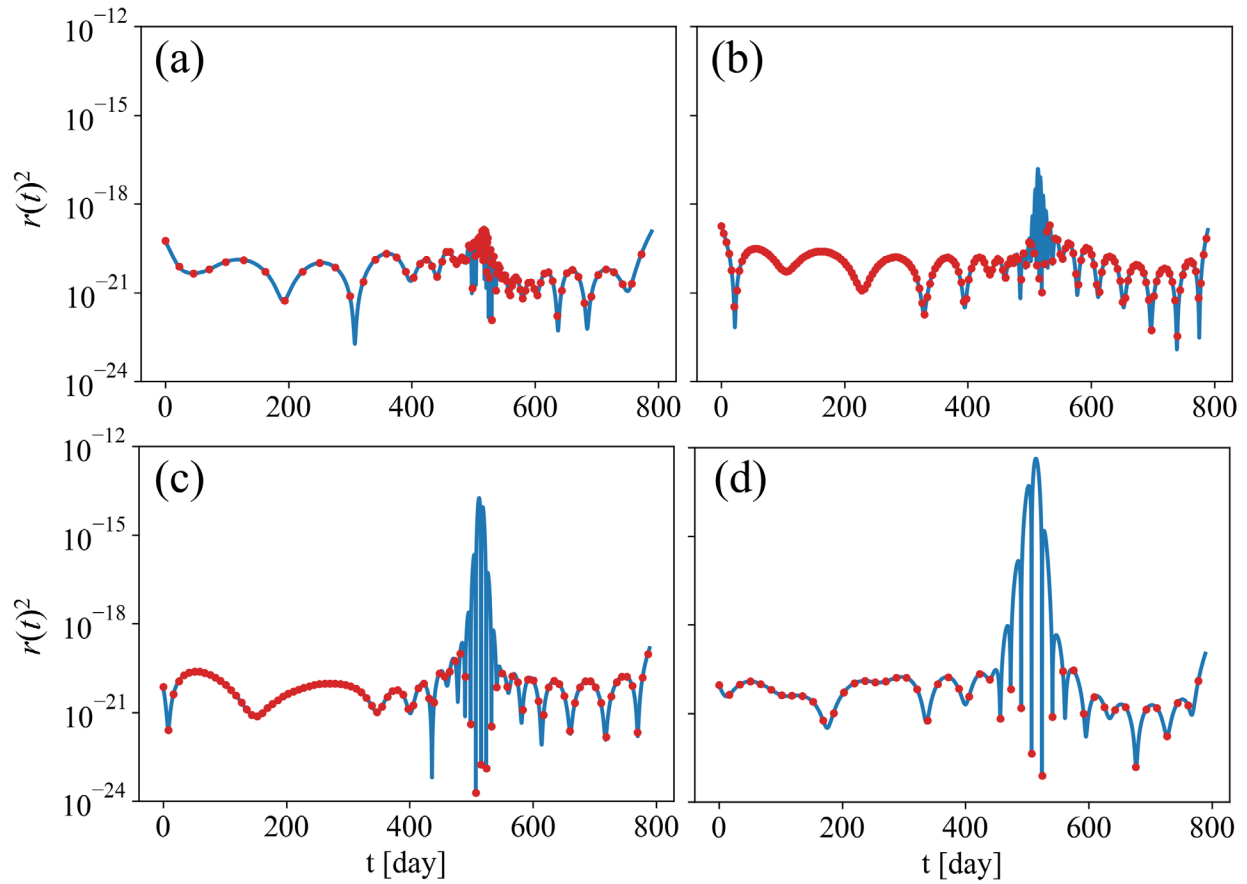
308

309 Next, we solved the spring-slider problem using PINNs, varying the number of equidistant
 310 collocation points, and discussed the relationship between the number of collocation points and
 311 the RE . In principle, increasing the number of collocation points enhances accuracy but slows
 312 down the computation speed. Thus, we explored the level of accuracy we could achieve in training
 313 the neural networks with fewer collocation points. We employed 94 and 47 equidistant collocation

314 points corresponding to intervals of 200 and 400 h, respectively, while we used 187 equidistant
315 collocation points with intervals of 100 h in the previous section.

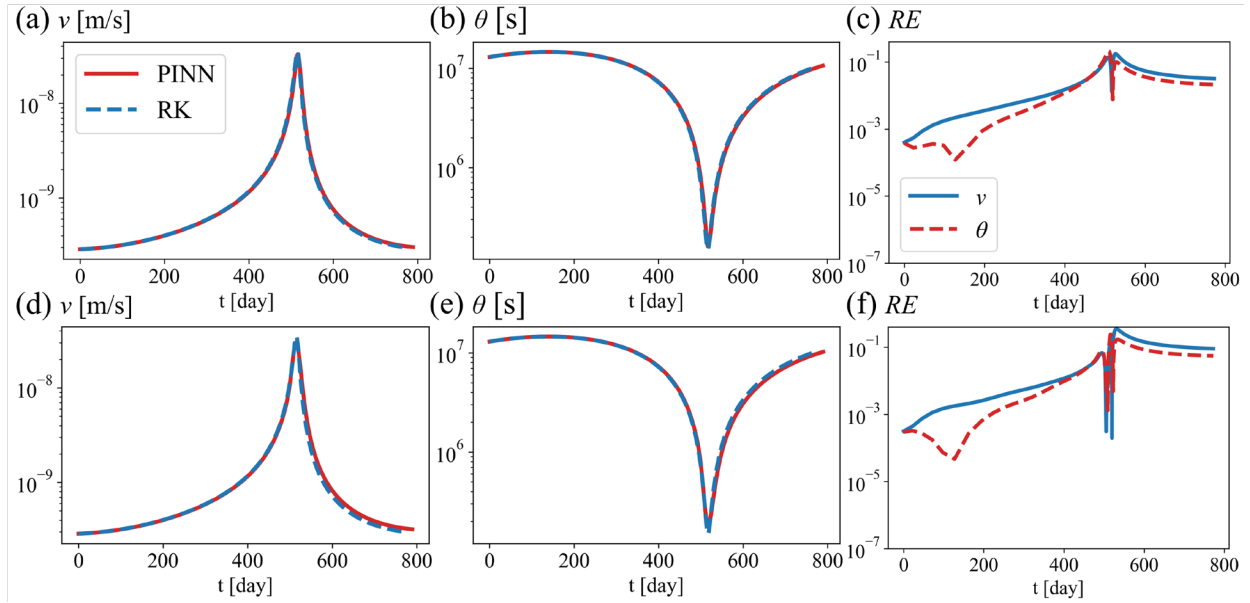
316 The results indicate that we can accurately model the temporal evolution of fault slip even
317 with fewer collocation points (Figures 6a, 6b, 6d, and 6e). The neural network parameters were
318 optimized after 6,492 iterations with the loss function of $L_{ini} = 1.51 \times 10^{-7}$ and $L_{ode} = 2.04 \times 10^{-6}$ in
319 the case of 200 h equidistant collocation points. For the case of 400 h equidistant collocation points,
320 the iteration increased to 9,942, and the loss function is $L_{ini} = 9.41 \times 10^{-8}$ and $L_{ode} = 1.45 \times 10^{-6}$. A
321 decreasing number of collocation points results in larger RE values after the velocity peak time
322 (Figures 6c and 6f). The residuals of the governing equations at each time t (Figures 5c and 5d)
323 indicate that if there are fewer collocation points, the entire $r(t)^2$ is not optimized adequately, and
324 $r(t)^2$ locally increases, leading to worse RE values. However, even with the number of collocation
325 points reduced to 47 (Figure 6f), the maximum RE is 10^{-1} , which is noteworthy considering that
326 the number of collocation points is less than half of that in the non-equidistant collocation point
327 case. This result demonstrates the high interpolation ability of neural networks and suggests the
328 potential of PINNs for rapid computation with fewer collocation points in large-scale problems. It
329 is important to note that the computation speed of PINNs depends not only on the number of
330 collocation points but also on the number of iterations required for optimization convergence.

331



332

333 **Figure 5.** Time series of residuals of the governing equations $r(t)^2$ on (a) non-equidistant and (b–
 334 d) equidistant collocation points with time intervals of (b) 100, (c) 200, and (d) 400 h. The red
 335 points represent the collocation points.



336

337 **Figure 6.** Calculation results using equidistant collocation points with time intervals of (a–c) 200
 338 h and (d–f) 400 h. (a and b) The temporal evolution of (a) v and (b) θ calculated by PINNs (red
 339 line) and the RK method (blue line) for time intervals of 200 h. (c) RE of v and θ . (d–f) Same as
 340 (a–c) but for time intervals of 400 h.

341

342 In summary, the relationship between the number of collocation points and calculation
 343 accuracy can be understood as follows. Firstly, fewer collocation points require long range
 344 interpolation of the residuals of the differential equation, $r(t)^2$, leading to insufficient optimization
 345 of $r(t)^2$. Secondly, large residuals of differential equations result in larger RE values.
 346 Understanding this relationship aids in determining the best collocation points for precise
 347 calculations. When considering problems involving modeling faster slip, more complex
 348 interpolation is required, as the temporal change in slip velocity is more drastic, thus demanding
 349 smaller time intervals for precise calculation. Solving stiff equations also requires smaller intervals
 350 because the residuals of differential equations significantly impact the solution of such equations.

351 Due to these reasons, applying PINNs to earthquake models, which involve rapid slips and require
352 solving very stiff equations, proves challenging. Therefore, in this study, we first calculated the
353 temporal evolution of SSE at the initial step of applying PINNs to fault slip modeling. However,
354 some recent studies have tried to develop techniques for solving stiff equations within the
355 framework of PINNs (e.g., Guo et al., 2022). Leveraging these methods will overcome the
356 challenges associated with using PINNs to model fast slips or earthquakes in the future.

357 It is notable that two strategies of non-equidistant and equidistant collocation points were
358 tested as endmembers to discuss the impact of collocation point sampling. There are some
359 discussions on the choices of collocation points when we do not know the evolution of physical
360 variables. For instance, Wu et al. (2023) reported that randomly sampled collocation points
361 perform better than equidistant collocation points. They also proposed the residual-based adaptive
362 sampling methods, and the implementation of such advanced sampling methods is useful for future
363 improvement.

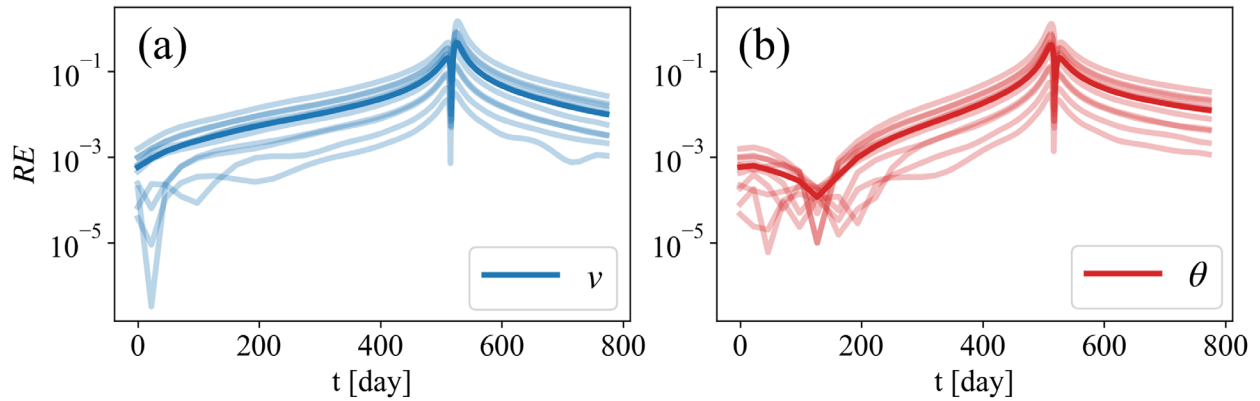
364

365 **3.3 Uncertainty quantification in forward problems**

366 In this subsection, we discuss the uncertainties of PINNs arising from the initial network
367 parameters. Recent studies have highlighted the importance of uncertainty quantification in PINNs
368 and have proposed a method for its calculation (e.g., Yang & Perdikaris, 2019). In this study, we
369 used normal Xavier initialization, and the initial values varied based on the random seed value.
370 Consequently, the optimized network parameters we eventually obtained are influenced by the
371 differences in the initial network parameters. We quantified the uncertainties of the converged
372 network parameters by repeating the optimization process with different values of initial network

373 parameters. Figure 7 represents the results optimized from 10 different initial network parameters
 374 using equidistant collocation points with the intervals of 100 h. The maximum relative error ranges
 375 from 10^{-2} to 10^{-1} , indicating uncertainties due to the selection of initial network parameters.

376



377

378 **Figure 7.** *RE* of (a) ν and (b) θ optimized from 10 different initial network parameters (thin lines)
 379 and their mean values (dark lines).

380

381 4 Inverse Problem

382 One of the significant advantages of PINNs is their inherent flexibility to extend to the
 383 inverse problems. In this section, we extend a forward problem for simulating fault slips described
 384 in Section 3 to an inverse problem for estimating unknown frictional parameters from the
 385 observation data.

386

387 **4.1 Method and synthetic data**

388 To extend to the inverse problems, we add a misfit term related to observed data to the loss
 389 function used in the forward problem, allowing us to simultaneously learn from the observation
 390 data and physical laws. We estimate three frictional parameters a , $a-b$, and d_c by giving synthetic
 391 data of the slip velocity including some errors as the observation data into the neural network.
 392 Although the frictional parameters control slip behavior on a fault, it is difficult to measure these
 393 parameters directly on the plate interface. Therefore, if PINNs can effectively solve this inverse
 394 problem, they would become a powerful tool for improving our understanding of fault properties.

395 We modified the loss function of Eq. (11) as follows:

$$396 \quad L = L_{ini} + L_{ode} + L_{data}, \quad (14)$$

397 where

$$398 \quad L_{data} = \frac{1}{N_{data}} \sum_{i=1}^{N_{data}} (p_{NN}(t_i) - p_{obs}(t_i))^2. \quad (15)$$

399 The third term in Eq. (14) represents a misfit term for observation data defined as the squared
 400 residuals between the observation data for slip velocity p_{obs} and the PINNs output p_{NN} , where N_{data}
 401 is the number of data points. Since the orders of magnitude of the frictional parameters vary, we
 402 defined the logarithm of the frictional parameters as $\alpha = \log a$, $\beta = \log(-(a-b))$ and $\gamma = \log d_c$. Note
 403 that this transformation implicitly assumes that $a-b$ is negative. We simultaneously optimized the
 404 frictional parameters α , β , and γ along with the neural network parameters by minimizing the loss
 405 function L (Figure 2). The true frictional parameters are set to be $a = 1.0 \times 10^{-4}$, $a-b = -1.0 \times 10^{-5}$,
 406 and $d_c = 5.0 \times 10^{-3}$ [m], as used in the previous forward problem. The first-guess values of the
 407 frictional parameters are set to be $a = 1.0 \times 10^{-3}$, $a-b = -1.0 \times 10^{-6}$, and $d_c = 5.0 \times 10^{-2}$ [m], assuming

408 a prior knowledge of the frictional parameters ranging from $\times 0.1$ to $\times 10$ relative to true values.
409 We discussed these first-guess values in Section 4.3.

410 To verify whether we can estimate the frictional parameters using the PINN-based
411 approach, we utilized synthetic slip velocity data. We generated this synthetic data with the
412 constant time intervals by adding the observation error to the true values v_{true} . Hence, the synthetic
413 observation data v_{obs} is

$$414 \quad v_{obs} = (1 + Er) v_{true}, \quad (16)$$

415 Where Er is the observation error. In order to generate true values with different constant time
416 intervals, we utilized PINNs, allowing us to express the continuous function. As conventional
417 numerical calculation results are discrete, it was necessary to perform calculations again, based on
418 the specific times of interest whenever we wanted to obtain velocities at new time steps. To avoid
419 this, we trained the neural network by providing the initial conditions, the governing equations,
420 and the results calculated by the RK method. Notably, we used the results of conventional
421 numerical calculations to achieve more precise training, although this is not strictly necessary to
422 train the PINNs. As a result, the obtained neural network is a continuous function that represents
423 the solution to this problem, enabling us to obtain the velocity at any arbitrary time without
424 recalculating the solution. In other words, we can interpolate the discrete outputs of conventional
425 numerical calculations using the PINN-based approach. We assume the observation error Er
426 follows a Gaussian distribution with a mean of zero and standard deviations of $\sigma_{er} = 0.1$ or 0.25 .
427 Time intervals of the observation data are set to be 100, 200, and 400 h.

428 In this section, we employ equidistant collocation points with intervals of 100 h. Training
429 is finished when the change of the frictional parameters per one optimization step becomes smaller
430 than the threshold value of 10^{-5} .

431

432 **4.2 Results**

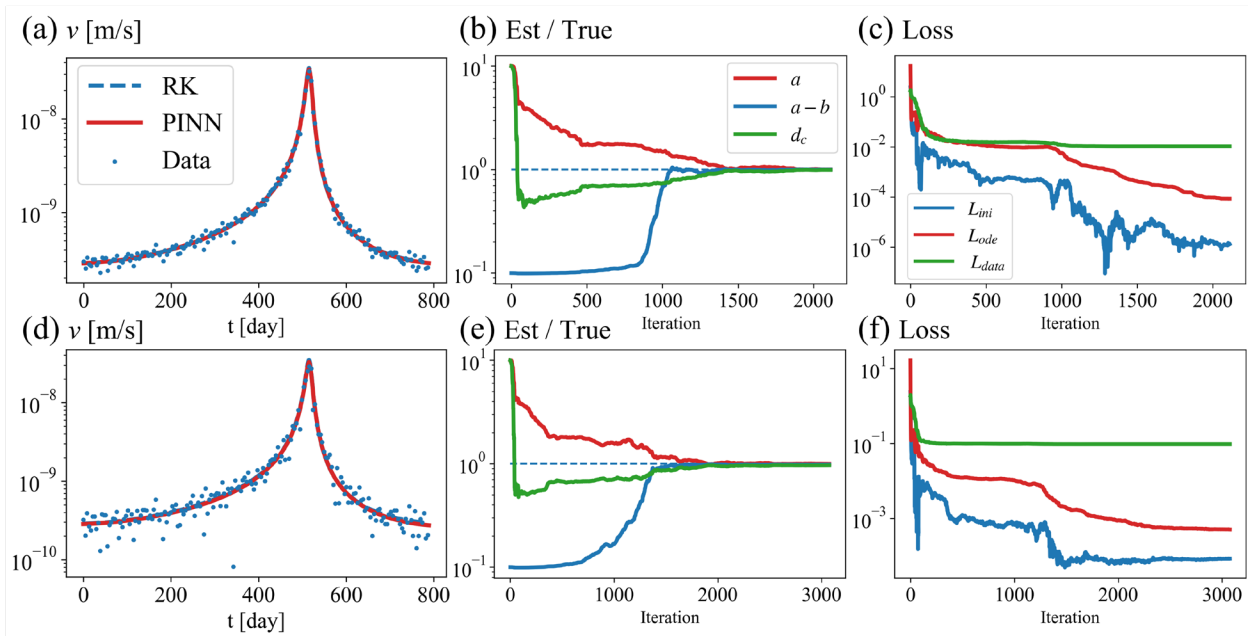
433 Figure 8 and Table 1 summarize the results of the PINNs outputs and the optimized
434 frictional parameters when we use the observation data with intervals of 100 h. The neural network
435 can obtain an output that fits the data well by solving the differential equations (Figures 8a and
436 8d), and it retrieved the true frictional parameters (Figures 8b, 8e, and Table 1). We successfully
437 optimized the frictional parameters with residuals smaller than 3.7 % compared to the true values.
438 These results indicate that the PINN-based approach is useful for estimating the frictional
439 parameters in inverse problems.

440 When using the synthetic slip velocity data with $\sigma_{er} = 0.1$, the network parameters and the
441 frictional parameters were simultaneously optimized after 2,113 iterations (Figure 8c). All terms
442 in the loss functions were reduced by learning the physical laws and observation data, ultimately
443 reaching $L_{ini} = 1.31 \times 10^{-6}$, $L_{ode} = 8.49 \times 10^{-5}$, and $L_{data} = 1.05 \times 10^{-2}$. In the case of $\sigma_{er} = 0.25$, the
444 optimization was converged after 3,075 iterations and the loss functions of $L_{ini} = 8.31 \times 10^{-5}$, L_{ode}
445 $= 5.01 \times 10^{-4}$, and $L_{data} = 9.54 \times 10^{-2}$ (Figure 8f).

446 It is worth noting that L_{data} did not change significantly during the latter half of optimization
447 and ultimately converged to a relatively large value compared to L_{ini} and L_{ode} due to the observation
448 error. Even if the PINNs outputs completely fit the result of conventional numerical calculations,
449 the values of L_{data} were 1.06×10^{-2} and 9.73×10^{-2} in the cases of $\sigma_{er} = 0.1$ and 0.25, respectively.

450 Therefore, this learning curve of L_{data} indicates how PINN estimated the frictional parameters.
 451 Initially, the neural network parameters were optimized to fit the observed velocity data, but at
 452 that time, the value of L_{ode} is large because the frictional parameters deviate from the true values,
 453 and they could not reproduce that result. Afterward, PINN searched for the frictional parameters
 454 that could decrease L_{ode} while fixing the velocity output. In other words, PINN initially tried to fit
 455 the data by discarding the governing equations, and then optimized the frictional parameters to
 456 comply with the physics. This disregard for physical laws at the initial stage of optimization is
 457 characteristic of the PINN-based inversion method.

458



459

460 **Figure 8.** (a–c) Results of parameter estimation using the velocity data with the observation error
 461 of $\sigma_{er} = 0.1$. (a) Temporal evolution of v calculated by PINNs (red line) and the RK method (blue
 462 line). Note that the blue line is invisible because it overlaps the red line. Blue points show the
 463 synthetic data including observation error. (b) Values of estimated frictional parameters
 464 normalized by their true values on each iteration. The red, blue, and green lines represent the value

465 of a , $a-b$, and d_c , respectively. (c) Learning curve for L_{ini} , L_{ode} , and L_{data} . The parameters converged
 466 after 2,113 iterations with $L_{ini} = 1.31 \times 10^{-6}$, $L_{ode} = 8.49 \times 10^{-5}$, and $L_{data} = 1.05 \times 10^{-2}$. (d–f) Same
 467 as (a–c) but for the case of $\sigma_{er} = 0.25$. The parameters converged after 3,075 iterations with $L_{ini} =$
 468 8.31×10^{-5} , $L_{ode} = 5.01 \times 10^{-4}$, and $L_{data} = 9.54 \times 10^{-2}$.

469

470 **Table 1.** True values, first-guess values, and estimated values of the frictional parameters using
 471 two synthetic data points. Error represents the relative error defined by $|\text{True value} - \text{Estimated}$
 472 $\text{value}| / |\text{True value}|$ and Ratio represents the ratio of first-guess value to the true value.

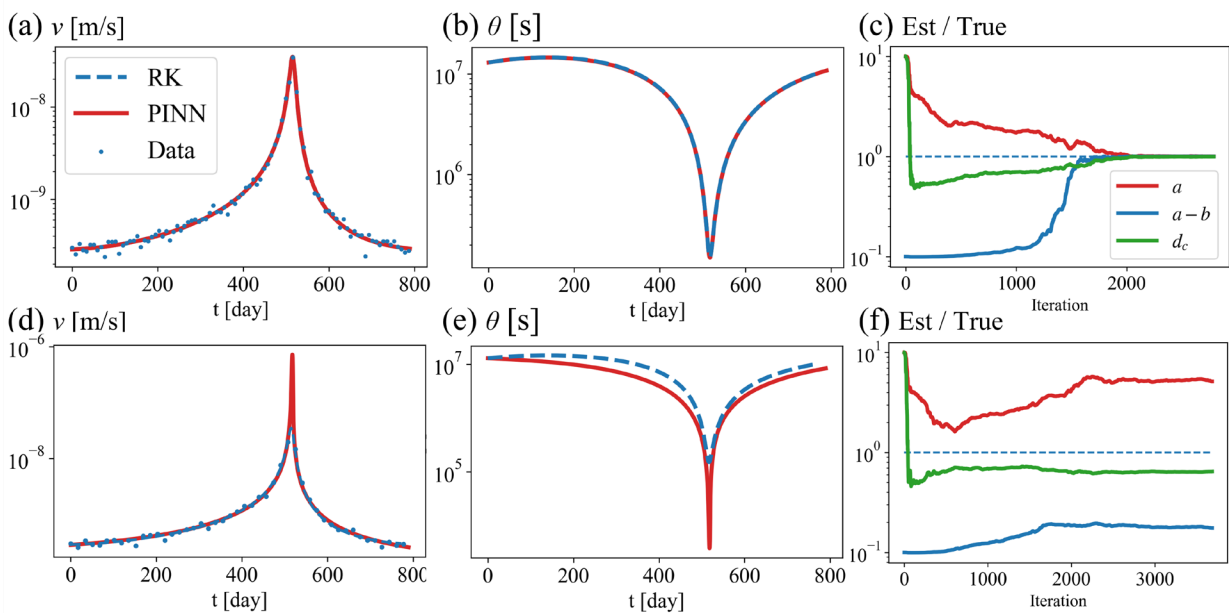
	True value	First-guess value	Estimated value (Noise: $\sigma_{er} = 0.1$)	Estimated value (Noise: $\sigma_{er} = 0.25$)
a	1×10^{-4}	1×10^{-3} Ratio: $\times 10$	1.004×10^{-4} Error: 0.4%	0.997×10^{-4} Error: 0.3%
$a-b$	-1×10^{-5}	-1×10^{-6} Ratio: $\times 0.1$	-0.998×10^{-5} Error: 0.1%	-0.980×10^{-5} Error: 2.0%
d_c [m]	5×10^{-3}	5×10^{-2} Ratio: $\times 10$	4.945×10^{-3} Error: 1.1%	4.817×10^{-3} Error: 3.7%

473

474 Figure 9 summarizes the results of the PINNs outputs and the optimized frictional
 475 parameters obtained from the observation data with intervals of 200 and 400 h, considering a
 476 standard deviation of $\sigma_{er} = 0.1$. It is important to note that while it is possible to estimate the
 477 frictional parameters from the observation data with fewer data points, insufficient data points can
 478 lead to inaccurate parameter retrieval. As anticipated, when intervals are 200 h, the true frictional
 479 parameters can be successfully estimated (Figure 9c). However, when intervals are extended to
 480 400 h, the estimate of the true frictional parameters fails (Figure 9f). With the estimated frictional

481 parameters in the case of 400 h data, the system behaves more drastically, resulting in a peak
 482 velocity larger than the true slip velocity (Figure 9d). This discrepancy arises due to the limited
 483 number of data points available near the peak velocity. Consequently, when using fewer data
 484 points, we are unable to adequately constrain the frictional parameters, highlighting a limitation
 485 imposed by the model. To ensure reliable estimations of the frictional parameters, it is essential to
 486 employ a sufficient amount of data, aligning with our intuitive understanding of the problem.

487



488

489 **Figure 9.** (a–c) Results of parameter estimation using the velocity data with time intervals of 200
 490 h. (a and b) Temporal evolution of (a) v and (b) θ calculated by PINNs (red line) and the RK
 491 method (blue line). Note that the blue line is invisible because it overlaps the red line. Blue points
 492 represent the synthetic data points including the observation errors. (c) Values of estimated
 493 frictional parameters normalized by their true values on each iteration. The red, blue, and green
 494 lines represent the values of a , $a-b$, and d_c , respectively. (d–f) Same as (a–c) but for the case with
 495 time intervals of 400 h.

496

497 **4. 3 Uncertainty quantification in inverse problems**

498 Quantifying the uncertainties of estimated frictional parameters is essential for evaluating
499 the robustness of the PINN-based inversion method. Additionally, this uncertainty analysis enables
500 the evaluation of uncertainties associated with the resulting slip velocities, which is crucial for
501 understanding the relationship between estimated frictional parameters and slip motion (Ito et al.,
502 2022). To achieve this, we performed the optimization process multiple times using different first-
503 guess values for the frictional parameters and various initial neural network parameters.

504 We trained the neural networks using eight different first-guess values (cases A–H) for the
505 frictional parameters, as presented in Table 2. These values cover a range from $\times 0.1$ to $\times 10$ relative
506 to the true values, assuming some prior knowledge of the frictional parameters. In each case, the
507 optimization process was repeated using 10 different initial neural network parameters to estimate
508 the frictional parameters. The neural networks were trained until the change in frictional
509 parameters per optimization step became smaller than a reference value of 10^{-5} and L_{ode} was less
510 than 10^{-3} . Synthetic data with a noise level of $\sigma_{er} = 0.1$ and intervals of 100 h were utilized.

511 Figure 10a illustrates the estimated values for each iteration across all eight cases. Although
512 the optimization trajectories vary depending on the first-guess values, it was observed that in all
513 cases, the estimated parameters eventually converged to the true values. Upon closer examination
514 of each trajectory, it was noticed that d_c reaches $\sim 50\%$ of the true values shortly after the start of
515 optimization in all cases. This result suggests that estimating the order of magnitude of d_c from the
516 observation data is relatively straightforward, and the gradient of the loss function with respect to
517 d_c is larger compared to the gradients with respect to other frictional parameters. Except for cases

518 E and F, respective trajectories of the 10 optimizations are relatively similar. However, the
519 trajectories of cases E and F differed depending on the initial values of the neural networks.
520 Furthermore, the trajectories of cases A–B, and cases C, D, G–H were comparable to each other.
521 These findings indicate that the gradients of the loss function with respect to frictional parameters
522 are small when the first-guess values of a are small, and they are large when the first-guess values
523 of a – b are large. Conversely, the gradients are relatively large in other cases.

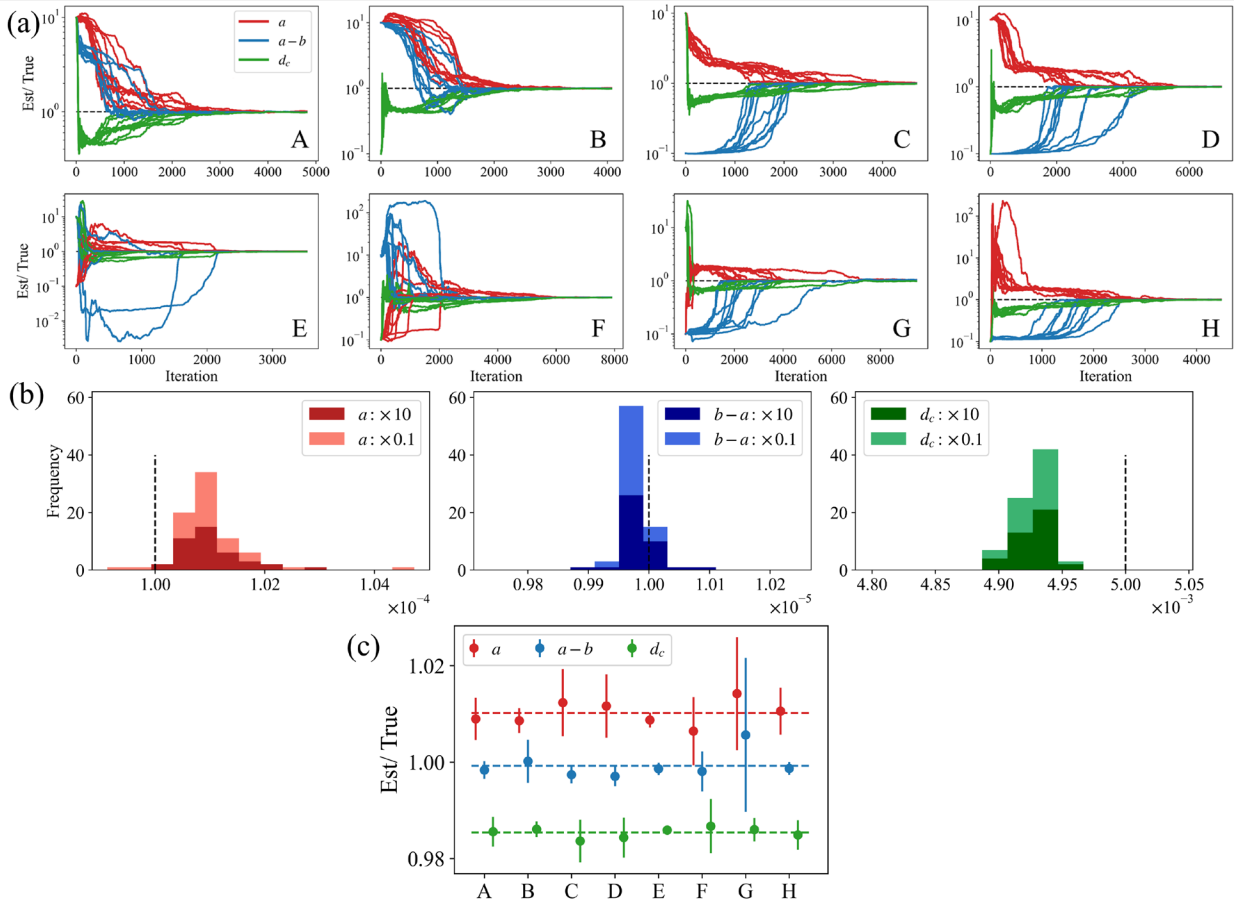
524 Figure 10b represents the distribution of all estimated parameters, with their means and
525 standard deviations shown in Table 3. The residuals of the estimated parameters reach up to 1.5%,
526 and the standard deviations are as large as 0.66% of the true values. The uncertainties of the
527 optimized parameters themselves are similar for all three frictional parameters. Specifically
528 focusing on a and d_c , the residuals of the estimated parameters are larger than their standard
529 deviations. This suggests that these discrepancies are primarily attributed to observation errors
530 rather than the effect of initial parameters in the PINNs.

531 Figure 10c depicts the means and standard deviations of the estimated parameters for all
532 cases. The variations in the means of estimated parameters, influenced by different first-guess
533 values, are smaller compared to the variations caused by variations in the initial values of neural
534 network parameters. This indicates that the choice of first-guess values for the frictional
535 parameters does not significantly impact the estimation results. In summary, the estimated
536 parameters are not significantly influenced by the first-guess values of initial parameters, despite
537 the fact that the optimization trajectories are affected by the first-guess values.

538

539 **Table 2.** First-guess values using in frictional parameter estimation.

	Case A	Case B	Case C	Case D	Case E	Case F	Case G	Case H
a	$\times 10$	$\times 10$	$\times 10$	$\times 10$	$\times 0.1$	$\times 0.1$	$\times 0.1$	$\times 0.1$
$a-b$	$\times 10$	$\times 10$	$\times 0.1$	$\times 0.1$	$\times 10$	$\times 10$	$\times 0.1$	$\times 0.1$
d_c	$\times 10$	$\times 0.1$	$\times 10$	$\times 0.1$	$\times 10$	$\times 0.1$	$\times 10$	$\times 0.1$



540

541 **Figure 10.** (a) Trajectories of estimated frictional parameters from the 10 different initial network

542 parameters in cases A–H presented in Table 2, normalized by the true values. The red, blue, and

543 green lines represent the values of a , $a-b$, and d_c , respectively. (b) The distribution of the estimated

544 frictional parameters in all cases. Dark and light colors express the results starting the optimization

545 process from smaller and larger first-guess values. The dashed lines indicate the true values. (c)

546 Means of estimated frictional parameters in each case with their uncertainties. The length of the

547 error bar indicates the standard deviation for each case and the dashed lines represent the means
 548 of estimated frictional parameters for all cases.

549

550 **Table 3.** Means and standard deviations of the estimated frictional parameters. The Error
 551 represents the relative error defined by $|\text{True value} - \text{Estimated value}| / |\text{True value}|$. The Ratio
 552 represents the standard deviation normalized by the true values.

	a	$a-b$	$d_c[\text{m}]$
Mean	1.010×10^{-4} Error: 1.0%	-0.999×10^{-5} Error: 0.1%	4.927×10^{-3} Error: 1.5%
Standard deviation	6.6×10^{-7} Ratio: 0.66%	6.4×10^{-8} Ratio: 0.64%	1.7×10^{-5} Ratio: 0.34%

553

554 5. Prediction of SSE evolution

555 For fault slip monitoring, it is crucial to predict the future temporal evolution of fault slip
 556 from the observation data. In this section, we attempt to estimate the frictional parameters from
 557 the observation data for an observation period shorter than the whole cycle of SSE and predict
 558 subsequent slip evolution.

559

560 5.1 Method

561 In Section 4, we estimated the frictional parameters from observation data over a full cycle
 562 (~800 days) by optimizing the neural network parameters and the frictional parameters to minimize
 563 the loss function. In this section, we consider situations where slip velocities are partially observed,

564 meaning that SSE is currently ongoing, and we aim to predict its future evolution. This can be
565 achieved simply by changing the data period in the loss function on observation data L_{data} (Eq.
566 (15)) and by optimizing the neural network parameters and the frictional parameters utilizing the
567 same loss function L (Eq. (14)). The collocation points are set at a constant time intervals of 100
568 h during one cycle, which is the same setting used in Section 4.

569 In this section, we use the observation data for the initial 400, 500, and 600 days of one
570 cycle. The data period of 400 days corresponds to the timing before the slip velocity reaches the
571 value of the loading velocity, v_{pl} ($\sim 1.58 \times 10^{-9}$ [m/s]). We attempt to predict when the next SSE
572 will occur based on the observations before a large slip occurs. The 500-day data period is the
573 duration just before the slip velocity reaches its maximum, and we attempt to predict when the
574 observed ongoing SSE will terminate. The 600-day period indicates the duration after the slip
575 velocity decreases to the value of v_{pl} , and prediction from this data mainly focuses on estimating
576 the frictional parameters from observation data after SSE has occurred. We generated three noisy
577 synthetic data with a standard deviation of $\sigma_{er} = 0.1$ and intervals of 100 h, following the method
578 described in Section 4.1.

579 We optimized the neural network and frictional parameters using eight different first-guess
580 values (cases A-H) and repeated the optimization with 10 different initial parameters. The neural
581 networks were trained until the change in the frictional parameters per optimization step was less
582 than the threshold value of 10^{-6} or the iteration reached 20,000. Considering the difficulty of
583 training due to a small number of data, the threshold value was set as 10^{-6} , which is smaller than
584 the value of 10^{-5} utilized in Section 4.

585

586 5.2 Results and discussions

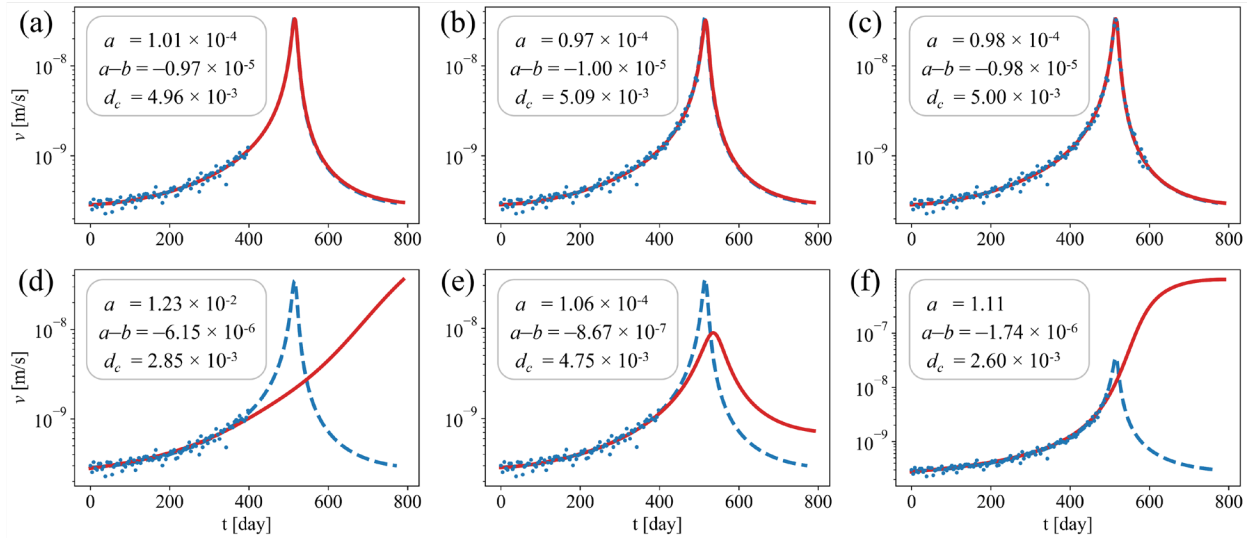
587 Figures 11a–c demonstrate the cases where future slip evolutions were successfully
588 predicted using the data for 400, 500, and 600 days, respectively. Even when we use observation
589 data for a shorter period such as 400 days, we succeeded in estimating the frictional parameters
590 and predicting the temporal evolution of SSE well. However, we sometimes failed in parameter
591 estimation as shown in Figures 11d–f. Figure 12 shows the histograms of all the estimated
592 parameters from each observation data set. Focusing on the distribution of estimated parameters
593 using observation data for 400 days, we can find a peak that is far from the true values, and the
594 ratio of successful results is ~35%. Conversely, when using longer observation data, the frequency
595 at the true values gradually increases, and the success ratio increases to ~50% and ~98% for the
596 case of 500 and 600 days, respectively.

597 These results are interpreted as follows: Observation data for shorter periods do not
598 sufficiently constrain the appropriate frictional parameters. As a result, depending on the first-
599 guess value of the frictional parameters and initial neural network parameters, optimized
600 parameters are likely to converge to incorrect values, resulting in inaccurate predictions. Figure 12
601 indicates that the success ratio dramatically increases when we use observation data for 600 days,
602 suggesting that the observation data after the peak time of slip velocity are important to constrain
603 the frictional parameters. The difficulty in parameter estimation prior to the SSE peak time has
604 also been pointed out in the data-assimilation approach (Fujita, 2019) and is not exclusive to the
605 PINN-based approach. This is inherent in the physics of fault slip and poses a critical problem for
606 predicting fault slip evolution. Consequently, a stochastic approach is required to predict SSE
607 before it occurs and, in this study, we evaluated the probability distribution of estimated frictional
608 parameters by repeating the deterministic optimization with different initial values.

609 In this paper, we repeatedly referred to the uncertainties of PINNs in Sections 3.3, 4.3, and
610 5. For accurate uncertainty quantification of PINNs, Bayesian physics-informed neural networks
611 (B-PINNs) have been proposed (Yang et al., 2021), and in seismology, they have been applied to
612 hypocenter inversion (Izzatullah et al., 2022) and seismic tomography (Agata et al., 2023). B-
613 PINNs treat neural network parameters as stochastic variables, enabling us to calculate the
614 posterior probability parameters using Hamiltonian Monte Carlo or variational inference.
615 Therefore, the application of B-PINNs in fault slip monitoring will become a powerful tool to
616 evaluate the uncertainties of neural networks and estimated frictional parameters, enabling a more
617 accurate stochastic prediction of fault slip evolution.

618 Finally, we discuss the comparison between the PINN-based method and data assimilation.
619 Focusing on the computation cost in the forward calculation, the PINN-based method is inferior
620 to the data assimilation method. Using a single CPU (Intel Core i5, 1.70 GHz, 12 cores, 16
621 processors, and 16 GB memory), the calculation shown in Figure 3 took 244 seconds. This
622 computation time was longer than that for the Runge-Kutta method that can solve this problem in
623 less than 1 second. Generally, it is reported that the PINN-based method requires more
624 computation cost than the conventional numerical calculation method (Grossmann et al., 2023). In
625 the inversion, the calculation shown in Figure 8 (a-c) took 44 seconds. which is less than that of
626 forward calculation This lower computation cost in the inversion is the characteristic of PINN. The
627 computation cost here is still larger than that of data assimilation, however, considering more
628 computationally difficult problems such as 2D fault models, the calculation cost of inversion
629 would possibly be smaller than data assimilation methods. This is because numerical integration
630 used in data assimilation requires higher computation cost in the complex models. In addition,
631 focusing on the simplicity of coding, the PINN-based method is superior to the data assimilation

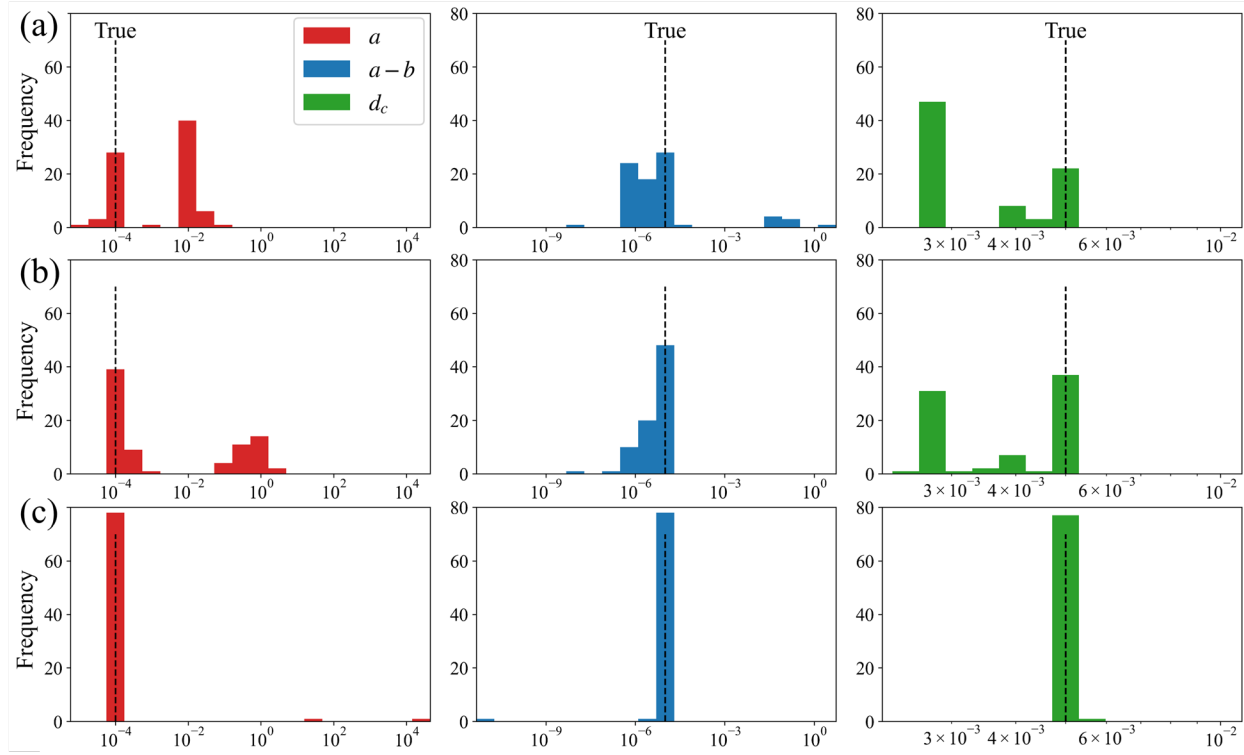
632 methods. In the PINN-based method, physics-based inversion could be done only by optimizing
 633 the defined loss function related to the observation and physics. This simple formulation enables
 634 us to extend to various physics models.



635

636 **Figure 11.** Examples of prediction results. The red and blue lines indicate the temporal evolution
 637 of v calculated by PINNs and the RK method. The blue points represent the synthetic data points,
 638 including observation errors. (a-c) Examples of successful prediction from observation data for (a)
 639 400, (b) 500, and (c) 600 days. (d-f) Examples of unsuccessful prediction from observation data
 640 for (d-e) 400 and (f) 500 days.

641



642

643 **Figure 12.** Histograms of the estimated frictional parameters from observation data for (a) 400,
 644 (b) 500, and (c) 600 days.

645

646 6. Conclusions

647 We proposed a new machine learning-based method for simulating, estimating frictional
 648 parameters, and predicting fault slips, and validated the effectiveness of this approach on slow slip
 649 events in a spring-slider system. In the forward simulation, PINNs accurately reproduced the
 650 temporal evolution of SSE, and the appropriate selection of collocation points played a crucial role
 651 in interpolating the residuals of equations. In frictional parameter estimation, the PINN-based
 652 approach successfully estimated the frictional parameters regardless of the first-guess values when
 653 using observation data for one cycle. For fault slip prediction, we achieved the evaluation of the

654 probability of future fault slip using the PINN-based approach, and the likelihood of accurate fault
655 slip prediction increased with longer observation periods. These results indicate that the PINN-
656 based approach is highly effective for simulating fault slips, estimating frictional parameters, and
657 predicting subsequent fault slips based on estimated parameters. Therefore, we strongly believe
658 that PINNs have tremendous potential as a powerful tool for fault slip monitoring.

659

660 **Open Research**

661 Python code developed in this study is available via <https://doi.org/10.5281/zenodo.8405977>
662 (Fukushima., 2023).

663

664 **Acknowledgments**

665 This work was supported by the MEXT Project for Seismology toward Research Innovation with
666 Data of Earthquake (STAR-E) [Grant Number JPJ010217] and by the JSPS KAKENHI [Grant
667 Numbers 18K03779, 21K03694, 23H00466, and 23K03552]. The author Rikuto Fukushima
668 received the Seto Prize of the Geodetic Society of Japan, and this work was also supported by the
669 award.

670

671 **References**

672 Agata, R., Shiraishi, K., & Fujie, G. (2023). Bayesian seismic tomography based on velocity-space
673 Stein variational gradient descent for physics-informed neural network. *IEEE Transactions*
674 *on Geoscience and Remote Sensing*, 10.1109/TGRS.2023.3295414.

- 675 Dieterich, J. H. (1979). Modeling of rock friction 1. Experimental results and constitutive
676 equations. *Journal of Geophysical Research: Solid Earth*, 84, 2161–2168.
677 <https://doi.org/10.1029/JB084iB05p02161>
- 678 Fujita, M. (2019). Estimation of the frictional parameters and slip evolution on fault with the
679 ensemble Kalman filter: application to the Bungo long-term SSE (Master's thesis).
680 Graduate School of Science, Kyoto University, Japan (in Japanese)
- 681 Fukushima, R. (2023). star-e-tohoku/PINN_spring_slider: simulation and frictional parameter
682 estimation on slow slip events: October 4, 2023 Release (Version v1) [Software]. Zenodo.
683 <https://doi.org/10.5281/zenodo.8405977>
- 684 Glorot, X., & Bengio, Y. (2010). Understanding the difficulty of training deep feedforward neural
685 networks. *Proceedings of the Thirteenth International Conference on Artificial Intelligence
686 and Statistics*, 9, 249–256. <https://proceedings.mlr.press/v9/glorot10a.html>
- 687 Grossmann, T. G., Komorowska, U. J., Latz, J., & Schönlieb, C.-B. (2023). *Can Physics-Informed
688 Neural Networks beat the Finite Element Method?* *arXiv:2302.04107*.
689 <http://arxiv.org/abs/2302.04107>
- 690 Guo, J., Wang, H., & Hou, C. (2022). A Novel Adaptive Causal Sampling Method for Physics-
691 Informed Neural Networks. *arXiv preprint arXiv:2210.12914*.
692 <http://arxiv.org/abs/2210.12914>
- 693 Hirahara, K., & Nishikiori, K. (2019). Estimation of frictional properties and slip evolution on a
694 long-term slow slip event fault with the ensemble Kalman filter: numerical experiments.
695 *Geophysical Journal International*, 219(3), 2074–2096. <https://doi.org/10.1093/gji/ggz415>

- 696 Hirose, H., Hirahara, K., Kimata, F., Fujii, N., & Miyazaki, S. (1999). A slow thrust slip event
697 following the two 1996 Hyuganada earthquakes beneath the Bungo Channel, southwest
698 Japan. *Geophysical Research Letters*, 26(21), 3237–3240.
699 <https://doi.org/10.1029/1999GL010999>
- 700 Im, K., Saffer, D., Marone, C., & Avouac, J. P. (2020). Slip-rate-dependent friction as a universal
701 mechanism for slow slip events. *Nature Geoscience*, 13(10), 705–710.
702 <https://doi.org/10.1038/s41561-020-0627-9>
- 703 Ito, S., Kano, M., & Nagao, H. (2022). Adjoint-based uncertainty quantification for
704 inhomogeneous friction on a slow-slipping fault. *Geophysical Journal International*,
705 232(1), 671–683. <https://doi.org/10.1093/gji/ggac354>
- 706 Izzatullah, M., Yildirim, I. E., Waheed, U. B., & Alkhalifah, T. (2022). Laplace HypoPINN:
707 physics-informed neural network for hypocenter localization and its predictive uncertainty.
708 *Machine Learning: Science and Technology*, 3(4), 045001. [https://doi.org/10.1088/2632-](https://doi.org/10.1088/2632-2153/ac94b3)
709 [2153/ac94b3](https://doi.org/10.1088/2632-2153/ac94b3)
- 710 Kano, M., Miyazaki, S., Ishikawa, Y., Hiyoshi, Y., Ito, K., & Hirahara, K. (2015). Real data
711 assimilation for optimization of frictional parameters and prediction of afterslip in the 2003
712 Tokachi-oki earthquake inferred from slip velocity by an adjoint method. *Geophysical*
713 *Journal International*, 203(1), 646–663. <https://doi.org/10.1093/gji/ggv289>
- 714 Kano, M., Miyazaki, S., Ishikawa, Y., & Hirahara, K. (2020). Adjoint-based direct data
715 assimilation of GNSS time series for optimizing frictional parameters and predicting
716 postseismic deformation following the 2003 Tokachi-oki earthquake. *Earth, Planets and*
717 *Space*, 72(1). <https://doi.org/10.1186/s40623-020-01293-0>

- 718 Linka, K., Schäfer, A., Meng, X., Zou, Z., Karniadakis, G. E., & Kuhl, E. (2022). Bayesian Physics
719 Informed Neural Networks for real-world nonlinear dynamical systems. *Computer*
720 *Methods in Applied Mechanics and Engineering*.
721 <https://doi.org/10.1016/j.cma.2022.115346>
- 722 Liu, D. C., & Nocedal, J. (1989). On the limited memory BFGS method for large scale
723 optimization. *Mathematical Programming*, 45(1), 503–528.
724 <https://doi.org/10.1007/BF01589116>
- 725 Miyazaki, S., Segall, P., McGuire, J. J., Kato, T., & Hatanaka, Y. (2006). Spatial and temporal
726 evolution of stress and slip rate during the 2000 Tokai slow earthquake. *Journal of*
727 *Geophysical Research: Solid Earth*, 111(3). <https://doi.org/10.1029/2004JB003426>
- 728 Obara, K., & Kato, A. (2016). Connecting slow earthquakes to huge earthquakes. *Science*,
729 353(6296), 253–257. <https://doi.org/10.1126/science.aaf1512>
- 730 Okazaki, T., Ito, T., Hirahara, K., & Ueda, N. (2022). Physics-informed deep learning approach
731 for modeling crustal deformation. *Nature Communications*, 13(1).
732 <https://doi.org/10.1038/s41467-022-34922-1>
- 733 Raissi, M., Perdikaris, P., & Karniadakis, G. E. (2019). Physics-informed neural networks: A deep
734 learning framework for solving forward and inverse problems involving nonlinear partial
735 differential equations. *Journal of Computational Physics*, 378, 686–707.
736 <https://doi.org/10.1016/j.jcp.2018.10.045>
- 737 Rasht-Behesht, M., Huber, C., Shukla, K., & Karniadakis, G. E. (2022). Physics-informed neural
738 networks (PINNs) for wave propagation and full waveform inversions. *Journal of*
739 *Geophysical Research: Solid Earth*, 127(5). <https://doi.org/10.1029/2021jb023120>

- 740 Rice, J. R. (1993). Spatio-temporal complexity of slip on a fault. *Journal of Geophysical Research*,
741 98(B6), 9885. <https://doi.org/10.1029/93jb00191>
- 742 Ruina, A. (1983). Slip Instability and State Variable Friction Laws. *Journal of Geophysical*
743 *Research*, 88(B12), 10359–10370. <https://doi.org/10.1029/JB088iB12p10359>
- 744 Segall, P. (2010). *Earthquake and Volcano Deformation*. Princeton University Press.
745 <https://doi.org/10.1515/9781400833856>
- 746 Segall, P., Rubin, A. M., Bradley, A. M., & Rice, J. R. (2010). Dilatant strengthening as a
747 mechanism for slow slip events. *Journal of Geophysical Research: Solid Earth*, 115(B12).
748 <https://doi.org/10.1029/2010JB007449>
- 749 Smith, J. D., Azizzadenesheli, K., & Ross, Z. E. (2021a). EikoNet: Solving the Eikonal Equation
750 With Deep Neural Networks. *IEEE Transactions on Geoscience and Remote Sensing*,
751 59(12), 10685–10696. <https://doi.org/10.1109/TGRS.2020.3039165>
- 752 Smith, J. D., Ross, Z. E., Azizzadenesheli, K., & Muir, J. B. (2021b). HypoSVI: Hypocentre
753 inversion with Stein variational inference and physics informed neural networks.
754 *Geophysical Journal International*, 228(1), 698–710. <https://doi.org/10.1093/gji/ggab309>
- 755 Waheed, U.B., Haghghat, E., Alkhalifah, T., Song, C., & Hao, Q. (2021a). PINNeik: Eikonal
756 solution using physics-informed neural networks. *Computers & Geosciences*, 155, 104833.
- 757 Waheed, U. B., Alkhalifah, T., Haghghat, E., Song, C., & Virieux, J. (2021b). PINNtomo: Seismic
758 tomography using physics-informed neural networks. *arXiv preprint arXiv:2104.01588*
- 759 Wu, C., Zhu, M., Tan, Q., Kartha, Y., & Lu, L. (2023). A comprehensive study of non-adaptive
760 and residual-based adaptive sampling for physics-informed neural networks. *Computer*

- 761 *Methods in Applied Mechanics and Engineering*, 403, 115671.
762 <https://doi.org/10.1016/j.cma.2022.115671>
- 763 Yang, L., Meng, X., & Karniadakis, G. E. (2021). B-PINNs: Bayesian physics-informed neural
764 networks for forward and inverse PDE problems with noisy data. *Journal of Computational*
765 *Physics*, 425, 109913. <https://doi.org/10.1016/j.jcp.2020.109913>
- 766 Yang, Y., & Perdikaris, P. (2019). Adversarial uncertainty quantification in physics-informed
767 neural networks. *Journal of Computational Physics*, 394, 136–152.
768 <https://doi.org/10.1016/j.jcp.2019.05.027>
- 769 Yoshida, S., & Kato, N. (2003). Episodic aseismic slip in a two-degree-of-freedom block-spring
770 model. *Geophysical Research Letters*, 30(13), 1681.
771 <https://doi.org/10.1029/2003GL017439>